

MIT Open Access Articles

Seasonal Variation in the Correlation Between Anomalies of Sea Level and Chlorophyll in the Antarctic Circumpolar Current

The MIT Faculty has made this article openly available. **Please share** how this access benefits you. Your story matters.

Citation: Song, Hajoan, et al. "Seasonal Variation in the Correlation Between Anomalies of Sea Level and Chlorophyll in the Antarctic Circumpolar Current." *Geophysical Research Letters* 45, 10 (May 2018): 5011–19.

As Published: <http://dx.doi.org/10.1029/2017GL076246>

Publisher: American Geophysical Union (AGU)

Persistent URL: <https://hdl.handle.net/1721.1/124782>

Version: Author's final manuscript: final author's manuscript post peer review, without publisher's formatting or copy editing

Terms of use: Creative Commons Attribution-Noncommercial-Share Alike



Seasonal variation in the correlation between anomalies of sea level and chlorophyll in the Antarctic Circumpolar Current region

Hajoon Song¹, Matthew C. Long², Peter Gaube³, Ivy Frenger⁴, John Marshall¹, Dennis J. McGillicuddy Jr.

¹Department of Earth, Atmospheric and Planetary Sciences, Massachusetts Institute of Technology, Cambridge,

Massachusetts, USA

²Climate and Global Dynamics Laboratory, National Center for Atmospheric Research, Boulder, Colorado, USA

³Applied Physics Laboratory, University of Washington, Seattle, Washington, USA

⁴GEOMAR Helmholtz Center for Ocean Research Kiel, Kiel, Germany

⁵Department of Applied Ocean Physics and Engineering, Woods Hole Oceanographic Institution, Woods Hole,

Massachusetts, USA

Key Points:

- Satellite observations and an eddy-rich model show positively/negatively correlated anomalies of sea level and chlorophyll in summer/winter.
- In summer, higher/lower iron concentration in positive/negative sea level anomalies leads to higher/lower chlorophyll.
- In winter, deeper/shallower mixed layers in positive/negative sea level anomalies decrease/increase chlorophyll through light limitation.

Abstract

We analyze satellite observations and an eddy-rich ocean model to show that mesoscale phenomena, such as fronts and eddies, strongly influence chlorophyll (CHL) concentrations in the Southern Ocean, driving CHL anomalies of opposite sign in winter versus summer. In austral winter, deeper mixed layers in positive sea surface height (SSH) anomalies reduce light availability, leading to anomalously low CHL concentration. In austral summer with abundant light, however, higher iron concentration in positive SSH anomalies yields higher CHL concentrations. The budget analysis of the model shows that anomalous vertical mixing associated with the mesoscale makes iron supply to the summertime mixed layer differ. Features with a negative SSH anomaly exhibit the opposite tendencies: higher CHL concentration in winter and lower in winter. Our results suggest that modulation of iron supply, light availability and vertical mixing by mesoscale processes plays an important role in causing systematic variations in primary productivity.

1 Introduction

The ocean is rich in mesoscale phenomena. They account for more than 90% of the kinetic energy in the surface ocean [Ferrari and Wunsch, 2009], and are thought to play a critical role in transporting momentum, heat, and energy [Robinson, 1983; Wunsch, 1999; Xu *et al.*, 2014]. The mesoscale modulates marine ecosystems because it affects the physical and chemical environment for life in the ocean, influencing, for instance, nutrient supply and the diversity of phytoplankton populations [McGillicuddy *et al.*, 2007; Rodríguez *et al.*, 2001; Clayton *et al.*, 2016]. This modulation is clearly seen in chlorophyll (CHL). Anomalies of surface CHL, a proxy for phytoplankton biomass, are observed to be correlated with sea surface height (SSH) anomalies, a proxy for mesoscale phenomena, in many regions of the ocean [Gaube *et al.*, 2014; Chelton *et al.*, 2011]. Depending on the prevailing drivers, both positive and negative correlations between CHL and SSH can be expected. A wide range of mechanisms have been proposed by which the mesoscale modulates biogeochemistry, as reviewed in McGillicuddy [2016].

In situ and satellite observations have revealed mixed layer depth (MLD) modulation by mesoscale dynamics; deeper (shallower) MLDs are associated with positive (negative) SSH anomalies in the subtropical ocean [Gaube *et al.*, 2013; Dufois *et al.*, 2014] and also in the SO [Hausmann *et al.*, 2017]. While the influence of mesoscale dynamics on the MLD, nitrate, and CHL in the subtropical gyres has received some attention [Du-

fois et al., 2014, 2016], these processes remain under-studied in the SO, which is a region of major importance for biogeochemical cycling and air-sea carbon exchange. In much of the SO, the supply of iron and availability of light are key mediators of primary productivity [Boyd, 2002; Fauchereau et al., 2011]. During summer when sunlight is abundant, primary productivity is primarily limited by iron, which is depleted in the surface ocean and enriched at depth [Boyd and Ellwood, 2010]. In such conditions, introduction of iron-rich subsurface water through vertical mixing can enhance the primary productivity and increase CHL. In contrast, during the winter, deep convective mixing supplies iron to the upper ocean [Tagliabue et al., 2014], but simultaneously decreases mixed-layer-average light levels for photosynthesis [Nelson and Smith, 1991]. Fauchereau et al. [2011] find large spatial and temporal variability in the correlation between CHL and MLD, and propose vertical mixing as an important driver for the surface CHL perturbation through changes in limitation by either iron or light.

The systematic modulation of MLD and its link to factors limiting productivity motivates our study of the correlation between CHL and SSH on the mesoscale in the Southern Ocean (SO). First we report on observed correlations between anomalies of SSH and CHL in the SO, particularly along the Antarctic Circumpolar Current (ACC), which plays a fundamental role in the global overturning circulation of the ocean [Marshall and Speer, 2012] and is characterized by elevated eddy activity [Frenger et al., 2015; Rintoul, 2009], and then evaluate the influences of MLD modulation by mesoscale dynamics on the observed correlation. Our study shows that the modulation of MLD by the mesoscale is an important mechanism that affects phytoplankton communities in the SO by regulating light availability and iron supply. In winter, MLDs differ by a few tens of meter between positive and negative SSH anomalies and influence the light availability. Despite of a few meters difference of MLD between them in summer, iron supply through vertical mixing is higher in positive SSH anomalies than negative anomalies.

2 Seasonal correlation between anomalies of sea surface height and chlorophyll

We evaluate the role of mesoscale phenomena by considering SSH anomalies exceeding 5 cm, noting that such deviations in SSH include those driven by coherent eddy structures, as well as other mesoscale flow features (e.g., fronts and meanders). We only consider areas where bathymetry is deeper than 100 m in order to avoid the direct influence from shelf regions. The correlations of CHL and SSH anomalies ($\rho_{SSH',CHL'}$) along

the ACC are characterized by intense seasonality, as pointed out by *Frenger* [2013]. Our correlation analysis of satellite observations of ocean color and SSH anomalies reveals a positive $\rho_{SSH',CHL'}$ along the ACC in summer (January–March, Fig. 1a) and a negative $\rho_{SSH',CHL'}$ in winter (July–September, Fig. 1b; data sources and analysis procedure are described in Supplementary Information). In winter, the signal is not as strong nor as clear as in the summer, which may be due to the lower density of wintertime observations and generally lower net primary productivity.

To identify the mechanisms by which mesoscale processes in the ACC influence CHL, we examine the solution of an eddy-rich, global ocean model run at $1/10^\circ$ horizontal resolution coupled to a biogeochemical model (details can be found in Supporting Information). Encouragingly, the simulation largely reproduces the observed seasonality in $\rho_{SSH',CHL'}$ (Figs 1c-d), as well as SSH variability and mean surface CHL (Supplementary Fig. 1). There are broad areas of strongly positive $\rho_{SSH',CHL'}$ along the ACC and at its southern margins in summer, changing sign in winter, especially in the Indian and Pacific Ocean sectors. South of the ACC, correlations are noisier and observed and modeled correlations agree less, perhaps due to processes that are missing in the model, such as iron supply from melting sea ice, or possibly weaker observational constraints in the polar zone.

We examined $\rho_{SSH',CHL'}$ averaged zonally along the path of the ACC (defined by SSH isolines, see Supplementary Information) to elucidate seasonal patterns. Correlations are positive in the northern part of the ACC from January–June, then switch to negative until October (Fig. 2a). Observations indicate that the seasonality in the correlation is lagged further south; the model, however, shows a more consistent phasing over the meridional extent of the ACC region (Fig. 2b). In spite of this inconsistency, the simulation captures the major correlations in the ACC, justifying an examination of the simulation to identify the underlying mechanisms generating observed variability in mesoscale modulations of the CHL field.

3 Model Diagnosis

We hypothesize that oceanic mesoscale dynamics play an important role in the seasonality of $\rho_{SSH',CHL'}$ along the ACC by regulating the availability of light and iron supply and resulting in differing CHL responses in summer and winter. There is a positive

correlation between MLD and SSH anomalies in all seasons over most of the SO, suggesting that positive SSH anomalies have deeper mixed layers than those with negative SSH anomalies (Figs 1e,f and 2e). This MLD modulation is more intense and systematic in winter than in summer, evident in a larger MLD difference between positive and negative SSH anomalies and a higher correlation coefficient between anomalies of SSH and MLD (Figs 2e and 3a,b). The degree of MLD modulation increases with the size of the SSH anomaly. For example, the wintertime MLD difference between positive and negative SSH anomalies greater than 5 cm is 24 m; this difference increases to 55 m when SSH anomalies greater than 20 cm are considered. The simulated correlation between SSH anomalies and MLD, seasonality in MLD modulation and dependency of MLD anomaly on the SSH anomaly amplitude are consistent with observed variations of MLD in eddies, whereby anticyclones exhibit weaker stratification and deeper mixed layers than cyclones [Hausmann *et al.*, 2017].

In winter, light is the primary factor limiting productivity throughout the whole water column and iron limitation is of diminished importance (Fig. 3b). Since light is supplied at the surface and attenuates with depth, mixed-layer mean light (or photosynthetically active radiation; $\langle \text{PAR} \rangle$) declines with increasing MLD. We find that $\langle \text{PAR} \rangle$ is negatively correlated with SSH throughout the year (Fig. 2d) and is approximately 30% lower in positive SSH anomalies than negative ones in winter (Fig. 4c) and about 7% lower in summer (Fig. 4a). Hence deeper mixing in positive SSH anomalies decreases $\langle \text{PAR} \rangle$ experienced by phytoplankton in the mixed layer; it is this effect that has the potential to explain lower wintertime CHL in positive versus negative anomalies in SSH (Figs 3a,d).

In contrast, productivity is iron limited in the summer (Fig. 3b). The model simulation shows that positive SSH anomalies in the ACC have 30% more $\langle \text{Fe} \rangle$ than negative SSH anomalies in winter (Fig. 4c) and approximately 15% more in summer (Fig. 4a). A budget analysis for $\langle \text{Fe} \rangle$ (Figure 4b,d; see Supplemental Information for details) quantifies the various mechanisms of iron supply and removal. Iron is supplied to the mixed layer by lateral and vertical advection, vertical mixing, aeolian input of dust, and entrainment associated with changes in the MLD; it is consumed by phytoplankton uptake and removed via scavenging on sinking particulates. Among these processes, we find that the supply of iron by vertical mixing differs most between positive and negative SSH anomalies. Supply of iron by vertical mixing in positive SSH anomalies has a median value that is roughly 10% higher than in negative SSH anomalies when normalized by the mean

148 $\langle \text{Fe} \rangle$ in the ACC. The differences in other terms are small compared to that in the verti-
 149 cal mixing. Iron input from dust increases $\langle \text{Fe} \rangle$ but, as might be expected, the differences
 150 between positive and negative SSH anomalies are negligible. The biogeochemical sink is
 151 the largest in summer with slightly more loss of iron in positive SSH anomalies due to
 152 higher phytoplankton productivity.

153 The contribution from advection, including eddy-driven lateral advection via trap-
 154 ping and stirring, potentially plays a role regionally if iron concentrations increase equa-
 155 torward (i.e., warm anticyclonic features with anomalously high iron concentration and
 156 cold cyclonic features with lower iron concentration). The Atlantic Ocean sector has a
 157 clear increasing equatorward trend of iron concentration in both observations [Mawji *et al.*,
 158 2015] and the model (Supplementary Fig. 3), i.e. sufficiently large to make an effect. Yet,
 159 in the Indian and Pacific Ocean sectors, small meridional gradients in iron are reported in
 160 the spring/summer vertical section of iron from GEOTRACES Intermediate Data Product
 161 2014 [Mawji *et al.*, 2015]. Our simulation generally agrees with observations (See Supple-
 162 mentary Fig. 2), and also reveals a small summertime lateral gradient of the surface iron
 163 in the Indian and Pacific Ocean sectors, which remains unchanged even below the mixed
 164 layer (Supplementary Fig. 3a,b), consistent with the overall small difference of iron advec-
 165 tion between positive and negative SSH anomalies.

166 While the budget analysis confirms that vertical mixing is a dominant process sup-
 167 plying iron to the mixed layer of positive SSH anomalies, the mechanisms driving this en-
 168 hancement are complex. Iron concentrations are elevated both within and below the MLD
 169 (Figs 3a-c). This suggests that part of the enhanced vertical flux in positive SSH anoma-
 170 lies is attributable to a larger Fe reservoir underlying these features at depth. Indeed, both
 171 the observations and the model simulation suggest that MLD modulation by the mesoscale
 172 is relatively subtle in summer; thus, the enhanced vertical iron gradient in positive SSH
 173 anomalies (Fig. 3c) may be the primary feature driving differences in iron supply by ver-
 174 tical mixing—as opposed to mixed layer modulation. In any case, our model simulates
 175 a positive correlation between anomalies of SSH and iron averaged over the mixed layer
 176 ($\langle \text{Fe} \rangle$) (Fig. 2c).

4 Discussion

Our study emphasizes the importance of mesoscale processes affecting phytoplankton growth through modulation of the MLD and iron availability. Features with anomalously high SSH are characterized by deeper mixed layers while those with negative SSH anomalies have anomalously shallow MLD. These modulations affect light levels resulting in lower/higher chlorophyll in positive/negative SSH anomalies in winter. The MLD modulation by the mesoscale is also seen in summer, but the median MLD difference is less than 5 m along the ACC. Nevertheless, the MLD modulation and anomalous vertical gradient of iron together make iron supply by vertical mixing different in positive versus negative SSH anomalies and contribute to iron anomalies in the mixed layer. Our results suggest that anomalies in iron availability and light exposure associated with the mesoscale and the alternating role of iron and light limitation in summer and winter play a major role in explaining seasonally changing correlation between SSH and chlorophyll anomalies along the ACC (Figs. 3e,f).

In other highly dynamic regions of intense eddy activity such as the Gulf Stream or the Kuroshio Current, it is thought that eddies cause anomalies of CHL concentration primarily through eddy-driven advection of large-scale CHL gradients, i.e. stirring and trapping [Kouketsu *et al.*, 2015; Gaube *et al.*, 2014]. The meridional gradient of CHL suggests that advective mechanisms cannot be entirely ruled out in understanding the correlations along the ACC (Supplementary Figs 1c-d). While advection of chlorophyll plays a role in generating anomaly correlations, the seasonal sign switch of correlations cannot be explained based solely on advective mechanisms [I. Frenger, personal communication, 2017].

Our model-based results strongly suggest that the modulation of iron and light limitation by the mesoscale is a crucial mechanism driving CHL perturbations in the ACC region. In particular, the MLD modulation by the mesoscale in winter is the mechanism that have recently been identified as important also for nitrate supply in the subtropical gyres [Dufois *et al.*, 2016] and air-sea chlorofluorocarbon-11 exchange in the SO [Song *et al.*, 2015].

We report a higher level of iron in positive SSH anomalies along the ACC in both seasons. A possible explanation for higher iron in positive SSH anomalies in summer is preconditioning during winter. In winter when the MLD modulation is particularly intense, deeper mixed layers in positive SSH anomalies have considerably higher iron concentra-

tion than the shallower mixed layers of negative SSH anomalies. Anomalously high iron in positive SSH anomalies in winter is not heavily used due to the lack of sunlight, and subsequently may promote elevated primary productivity in summer. The mixed layer shoals rapidly after winter, but vertical mixing at the base of the mixed layer continues to entrain iron from the layer that was previously in the mixed layer during winter. Hence positive SSH anomalies have relatively iron-rich water below the summertime mixed layer compared to negative SSH anomalies, and this may contribute to differences in iron limitation among the two types of features. This explanation can be applied to well-formed and long-lived SSH anomalies whose lifespans are of the order of months (eddy).

Our study defines eddies based on SSH anomalies (> 5 cm) instead of the closed SSH contour as in other studies [Chelton *et al.*, 2007; Hausmann *et al.*, 2017]. Hence the correlation between SSH and chlorophyll anomalies includes not only coherent eddy structures but also mesoscale fronts and meanders. This may cause the MLD modulations computed in both the observations and the model to be weaker than those that would result from restricting our analysis to coherent structures, and thereby make the anomalous iron flux by vertical mixing stand out less.

Understanding the influence of mesoscale processes on vertical mixing and iron supply is important for more accurate estimation of SO's role in global carbon cycle. However, coarse resolution climate modeling systems on which current studies rely do not resolve the ocean's mesoscale. Such models cannot capture mixed layer modulation by the mesoscale, leading to as yet unknown biases in air-sea carbon dioxide flux. Quantifying the integrated effects of these phenomena on biological uptake and the supply of carbon rich water from depth is necessary to better understand the role of mesoscale on biogeochemical cycling in the SO.

Acknowledgments

The altimeter products were produced and distributed by Aviso (<http://www.aviso.altimetry.fr/>), as part of the Ssalto ground processing segment. The CHL observations are available through NASA MEaSUREs Ocean Color Product Evaluation Project (<ftp://ftp.oceancolor.ucsb.edu/>). Computational facilities have been provided by the Climate Simulation Laboratory, which is managed by CISL at NCAR. NCAR is supported by the National Science Foundation. The CESM source code is freely available at <http://www2.cesm.ucar.edu>. HS, JM and DJM were supported by the NSF MOBY project (OCE-1048926). DJM also acknowl-

edges support from NSF (OCE-1048897) and NASA (NNX13AE47G). In addition, PG acknowledges support from NSF (OCE-1558809) and NASA (NNX13AE47G, NNX16AH9G).

References

- Boyd, P. W. (2002), The role of iron in the biogeochemistry of the Southern Ocean and equatorial Pacific: a comparison of in situ iron enrichments, *Deep-Sea Res., Pt II*, 49(9–10), 1803–1821, doi:http://dx.doi.org/10.1016/S0967-0645(02)00013-9.
- Boyd, P. W., and M. J. Ellwood (2010), The biogeochemical cycle of iron in the ocean, *Nature Geoscience*, 3(10), 675–682.
- Chelton, D. B., M. G. Schlax, R. M. Samelson, and R. A. de Szoeke (2007), Global observations of large oceanic eddies, *Geophys. Res. Lett.*, 34, L15,606.
- Chelton, D. B., P. Gaube, M. G. Schlax, J. J. Early, and R. M. Samelson (2011), The Influence of Nonlinear Mesoscale Eddies on Near-Surface Oceanic Chlorophyll, *Science*, 334(6054), 328–332.
- Clayton, S., S. Dutkiewicz, O. Jahn, C. Hill, P. Heimbach, and M. J. Follows (2016), Biogeochemical versus ecological consequences of modeled ocean physics, *Biogeosciences Discussions*, 2016, 1–20, doi:10.5194/bg-2016-337.
- Dufois, F., N. J. Hardman-Mountford, J. Greenwood, A. J. Richardson, M. Feng, S. Herbet, and R. Matear (2014), Impact of eddies on surface chlorophyll in the South Indian Ocean, *J. Geophys. Res. Oceans*, 119, 8061–8077, doi:10.1002/2014JC010164.
- Dufois, F., N. J. Hardman-Mountford, J. Greenwood, A. J. Richardson, M. Feng, and R. J. Matear (2016), Anticyclonic eddies are more productive than cyclonic eddies in subtropical gyres because of winter mixing, *Science Advances*, 2(5), e1600,282–e1600,282.
- Fauchereau, N., A. Tagliabue, L. Bopp, and P. M. S. Monteiro (2011), The response of phytoplankton biomass to transient mixing events in the Southern Ocean, *Geophys. Res. Lett.*, 38, L17,601, doi:10.1029/2011GL048498.
- Ferrari, R., and C. Wunsch (2009), Ocean circulation kinetic energy: Reservoirs, sources, and sinks, *Annu. Rev. Fluid Mech.*, 41, 253–282, doi:10.1146/annurev.fluid.40.111406.102139.
- Frenger, I. (2013), On Southern Ocean eddies and their impacts on biology and the atmosphere, Ph.D. thesis, ETH Zurich, Zurich, Switzerland, doi:10.3929/ethz-a-009938120.
- Frenger, I., M. Münnich, N. Gruber, and R. Knutti (2015), Southern ocean eddy phenomenology, *Journal of Geophysical Research: Oceans*, 120(11), 7413–7449, doi:

- 10.1002/2015JC011047.
- Gaube, P., D. B. Chelton, P. G. Strutton, and M. J. Behrenfeld (2013), Satellite observations of chlorophyll, phytoplankton biomass, and Ekman pumping in nonlinear mesoscale eddies, *J. Geophys. Res. Oceans*, *118*, 6349–6370, doi:10.1002/2013JC009027.
- Gaube, P., D. J. McGillicuddy, Jr., D. B. Chelton, M. J. Behrenfeld, and P. G. Strutton (2014), Regional variations in the influence of mesoscale eddies on near-surface chlorophyll, *J. Geophys. Res. Oceans*, *119*, doi:10.1002/2014JC010111.
- Hausmann, U., D. J. McGillicuddy, Jr., and J. Marshall (2017), Observed mesoscale eddy signatures in Southern Ocean surface mixed-layer depth, *J. Geophys. Res. Oceans*, *122*, 617–635, doi:10.1002/2016JC012225.
- Kouketsu, S., H. Kaneko, T. Okunishi, K. Sasaoka, S. Itoh, R. Inoue, and H. Ueno (2015), Mesoscale eddy effects on temporal variability of surface chlorophyll *a* in the Kuroshio Extension, *J. of Oceanogr.*, *72*(3), 439–451.
- Marshall, J., and K. Speer (2012), Closure of the meridional overturning circulation through Southern Ocean upwelling, *Nature Geoscience*, *5*(3), 171–180.
- Mawji, E., et al. (2015), The GEOTRACES intermediate data product 2014, *Mar. Chem.*, *177*, 1–8, doi:https://doi.org/10.1016/j.marchem.2015.04.005.
- McGillicuddy, D. J., Jr. (2016), Mechanisms of Physical-Biological-Biogeochemical Interaction at the Oceanic Mesoscale, *Annu. Rev. Mar. Sci.*, *8*(1), 125–159.
- McGillicuddy, D. J., Jr., L. A. Anderson, N. R. Bates, T. Bibby, K. Buesseler, C. Carlson, C. Davis, C. Ewart, P. Falkowski, S. Goldthwait, D. Hansell, W. Jenkins, R. Johnson, V. Kosnyrev, J. Ledwell, Q. Li, D. Siegel, and D. Steinberg (2007), Eddy/wind interactions stimulate extraordinary mid-ocean plankton blooms, *Science*, *316*, 1021–1026.
- Nelson, D. M., and W. O. Smith, Jr. (1991), Sverdrup revisited: Critical depths, maximum chlorophyll levels, and the control of Southern Ocean productivity by the irradiance-mixing regime, *Limnology and Oceanography*, *36*(8), 1650–1661.
- Rintoul, S. (2009), Antarctic circumpolar current, in *Encyclopedia of Ocean Sciences (Second Edition)*, edited by J. H. Steele, second edition ed., pp. 178–190, Academic Press, Oxford, doi:http://dx.doi.org/10.1016/B978-012374473-9.00603-2.
- Robinson, A. R. (Ed.) (1983), *Eddies in Marine Science*, Springer Berlin Heidelberg, doi:10.1007/978-3-642-69003-7.

- 305 Rodríguez, J., J. Tintoré, J. T. Allen, J. M. Blanco, D. Gomis, A. Reul, J. Ruiz, V. Ro-
 306 dríguez, F. Echevarría, and F. Jiménez-Gómez (2001), Mesoscale vertical motion and
 307 the size structure of phytoplankton in the ocean, *Nature*, *410*(6826), 360–363.
- 308 Song, H., J. Marshall, P. Gaube, and D. J. McGillicuddy, Jr. (2015), Anomalous chloroflu-
 309 orocarbon uptake by mesoscale eddies in the Drake Passage region, *J. Geophys. Res.*
 310 *Oceans*, *120*, 1065–1078, doi:10.1002/ 2014JC010292.
- 311 Tagliabue, A., J.-B. Sallée, A. R. Bowie, M. Lévy, S. Swart, and P. W. Boyd (2014),
 312 Surface-water iron supplies in the Southern Ocean sustained by deep winter mixing,
 313 *Nature Geoscience*, *7*, 314–320, doi:10.1038/ngeo2101.
- 314 Wunsch, C. (1999), Where do ocean eddy heat fluxes matter?, *J. Geophys. Res.*, *104*,
 315 13,235–13,249.
- 316 Xu, C., X.-D. Shang, and R. X. Huang (2014), Horizontal eddy energy flux in the
 317 world oceans diagnosed from altimetry data, *Scientific Reports*, *4*, 5316, doi:
 318 10.1038/srep05316.

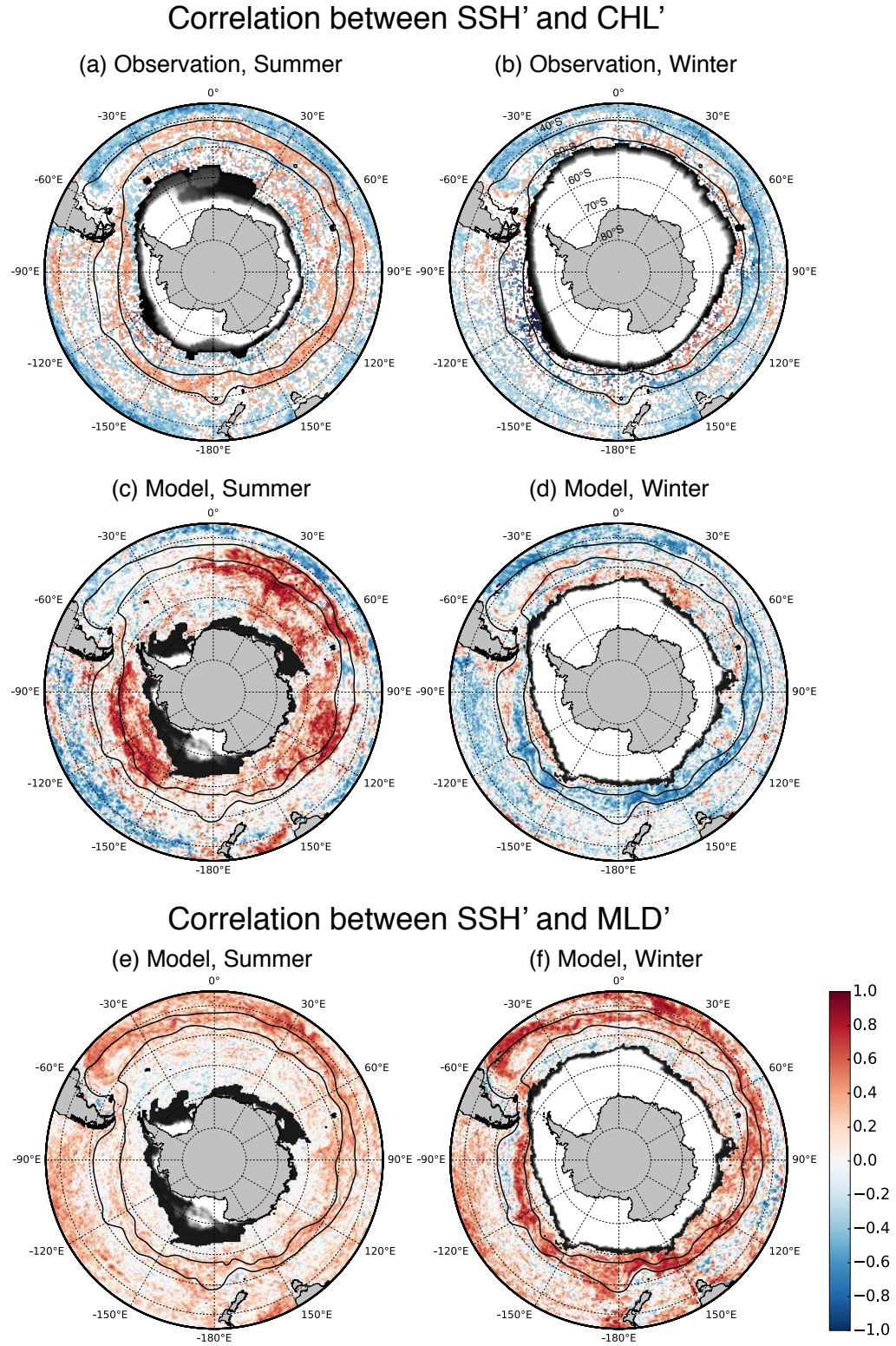


Figure 1. (Caption next pages.)

Figure 1. (Previous page.) The correlation coefficients between anomalies of sea surface height (SSH) and chlorophyll in the (a,b) satellite observations and (c,d) 1/10° ocean model are shown as pseudo-color images. The left and right columns show the (a,c) correlation for austral summer (January-March) and (b,d) austral winter (July-September), respectively. Black contours mark the sea level isolines of -20 cm and -80 cm that enclose the ACC. The masks in gray scale around Antarctica represent the sea-ice area fraction from the Hadley Centre Sea Ice and Sea Surface Temperature data set in (a,b) and from the model in (c,d). The sea-ice area fraction decreases from 1 to 0 as the color changes from white to black. The correlation coefficients between anomalies of SSH and mixed layer depth (MLD) in the eddy-rich model are also presented similarly in (e,f).

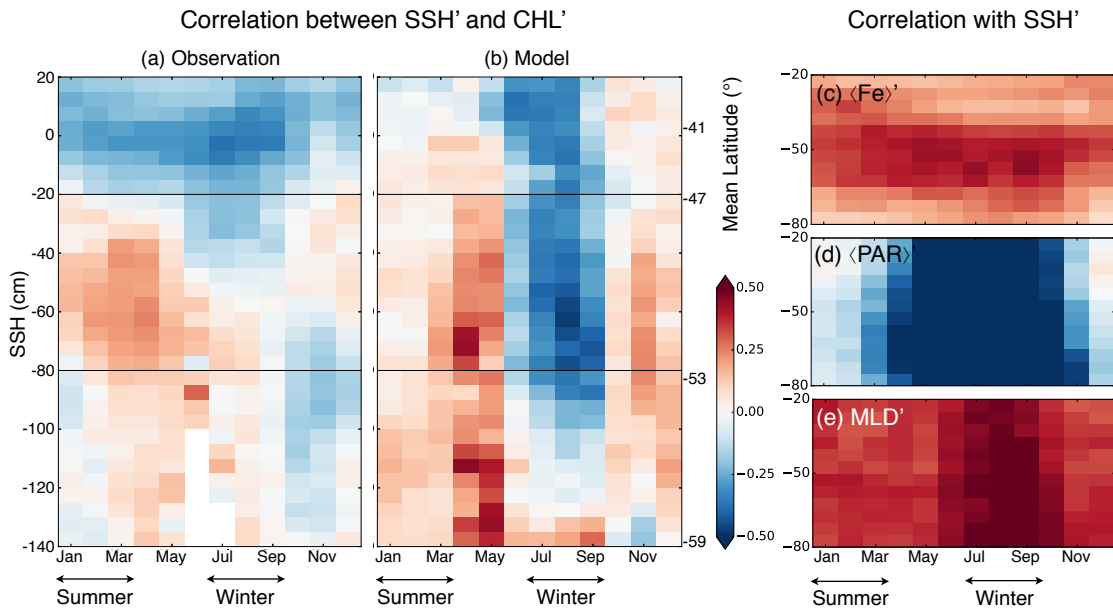


Figure 2. The correlation of anomalies in SSH and chlorophyll along SSH isolines in (a) observations and (b) model. The areas within two black lines at -80 cm and -20 cm approximate the ACC and correspond to the black contours in Figure 1. The equivalent latitude is shown on the right y-axis in (b). Panels on the right are the correlation coefficients of anomalies of the (c) iron and (d) light limiting factor averaged over the MLD, and (e) MLD with SSH anomalies. Correlations are statistically significant at the 99% confidence level.

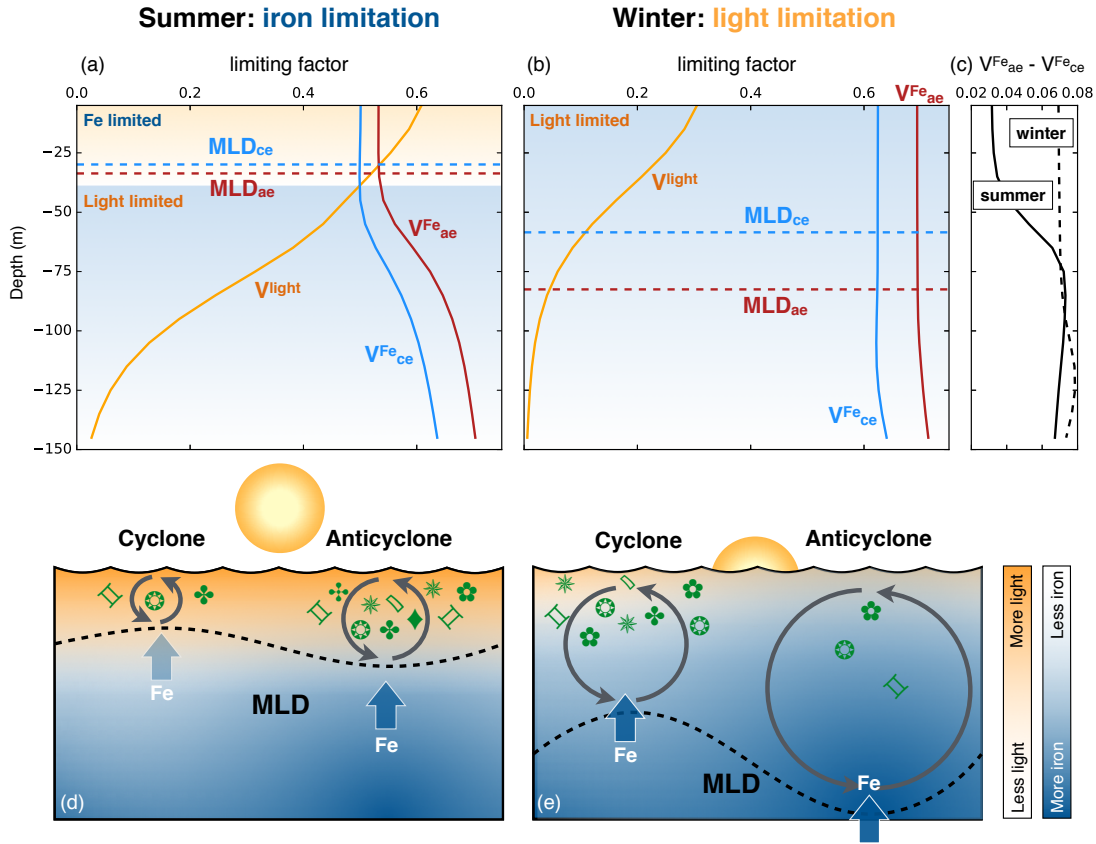


Figure 3. (a,b) The median vertical profiles of light limiting factor (marked by “ V^{light} ” in orange) and iron limiting factors for positive SSH anomalies (anticyclones marked by “ $V^{Fe_{ae}}$ ”) and negative SSH anomalies (cyclones marked by “ $V^{Fe_{ce}}$ ”) in the biogeochemical model averaged in the ACC. In summer, iron is the limiting factor for the primary productivity within the mixed layer, however, light limits primary productivity more below the mixed layer (a). The magnitude of limiting factor is inversely related to its’ affect on primary productivity, e.g., light is more important than iron concentration throughout the whole water column in winter (b). Blue and red dotted lines represent the median value for mixed layer depth (MLD) within negative (cyclones) and positive (anticyclones) SSH anomalies, respectively, in the ACC. Panel (c) displays the vertical profile of the iron limiting factor differences ($V^{Fe_{ae}} - V^{Fe_{ce}}$) in summer (solid line) and winter (dashed line). A diagram depicting the mesoscale modulation of MLD and its impact on phytoplankton biomass in two different seasons in the Southern Ocean are shown in panes (d) and (e). The brightness of the blue and orange shading represents the iron concentration and sunlight intensity, respectively. In summer, primary production is controlled by iron supply (blue arrows) and not light in the mixed layer (d). In winter, intensive vertical mixing enriches iron concentration near the surface, but low light availability limits primary production (e).

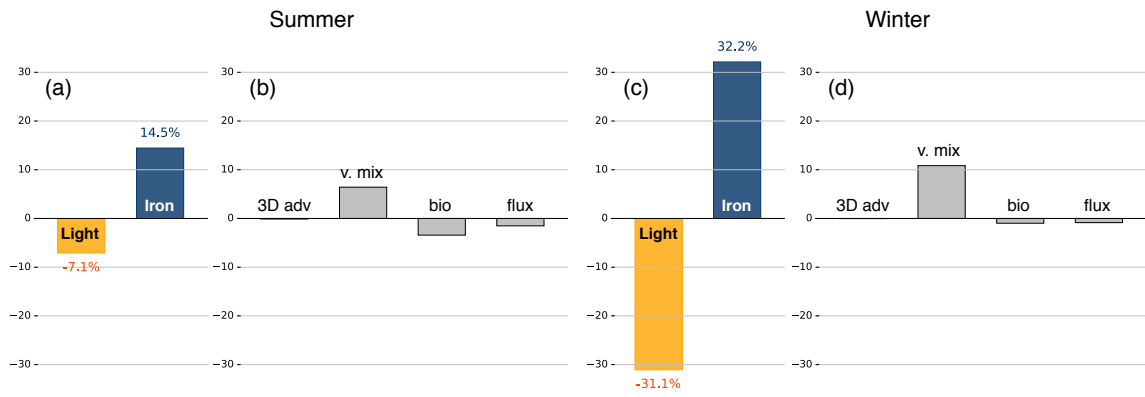


Figure 4. The bar plots in (a,c) represent the percentage differences in light level (yellow) and iron concentration (blue) in the mixed layer between positive (anticyclones) and negative (cyclones) SSH anomalies in summer and winter, respectively. The percentage differences between anticyclones and cyclones in various contribution to the iron averaged over the mixed layer are plotted in (b,d). Those contributions are 3-dimensional advection (3D adv), vertical mixing (v. mix), biogeochemical cycle (bio) and flux from dust (flux), and they are normalized by the averaged iron in the mixed layer.

Supporting Information for

“Mesoscale modulation of mixed layer depth and its impact on Southern Ocean chlorophyll”

Hajoon Song¹, Matthew C. Long², Peter Gaube³, Ivy Frenger⁴, John Marshall¹, Dennis J. McGillicuddy Jr.

¹Department of Earth, Atmospheric and Planetary Sciences, Massachusetts Institute of Technology, Cambridge,

Massachusetts, USA

²Climate and Global Dynamics Laboratory, National Center for Atmospheric Research, Boulder, Colorado, USA

³Applied Physics Laboratory, University of Washington, Seattle, Washington, USA

⁴GEOMAR Helmholtz Center for Ocean Research Kiel, Kiel, Germany

⁵Department of Applied Ocean Physics and Engineering, Woods Hole Oceanographic Institution, Woods Hole,

Massachusetts, USA

Satellite observations

The SSH anomaly fields were downloaded from Collecte Localis Satellites (CLS/AVISO) on a 1/4 degree grid for the 10 year period 1998 to 2007 at 7-day intervals. The near-surface chlorophyll concentration product comes from the Sea-Viewing Wide Field-of-View Sensor (SeaWiFS) project during the same period as the SSH anomaly. The Garver-Siegel-Maritorena (GSM) semi-analytical ocean color algorithm [Garver and Siegel, 1997; Maritorena et al., 2002; Siegel et al., 2002] was used to estimate CHL from ocean color measurements made by SeaWiFS. The log-transformed daily chlorophyll concentration estimates were averaged within the 1/4×1/4 degree grid to match the resolution of the SSH anomaly fields. The CHL fields were first \log_{10} transformed and then low-pass filtered using a loess smoother with a half-power cutoff of 2° in both latitude and longitude and 35-days in time onto. The resultant smoothed CHL fields have spatial and temporal resolution comparable with the SSH anomaly fields. The anomalies of the CHL fields were computed at each 7-day time step by high-pass filtering with a spatial loess smoother with a half-power cutoff of 6° in both latitude and longitude. The resulting anomalies are then transformed back to linear concentrations Campbell [1995]; Gaube et al. [2013] and $\rho_{SSH,CHL}$ is computed for each grid box as shown in Figures 1a,b. In addition, we com-

Corresponding author: H. Song, hajsong@mit.edu

puted $\rho_{SSH',CHL'}$ in SSH bins, *i.e.* approximately along streamlines as shown in Figure 2a (see also *Frenger* [2013]).

Model Simulations

The mechanisms generating observed $\rho_{SSH',CHL'}$ were examined using the Biogeochemical Elemental Cycling (BEC) model [*Moore et al.*, 2002, 2004, 2013] coupled to the ocean circulation component of the Community Earth System Model (CESM) with a resolution of 0.1° (less than 10 km in zonal direction in the Drake Passage). The total chlorophyll concentration is computed as the sum of chlorophyll of three phytoplankton functional groups whose biomasses are affected by the uptake of varied nutrients including iron, and grazing by zooplankton. The vertical mixing is estimated by the K-Profile Parameterization (KPP) mixing scheme [*Large et al.*, 1994] and we treated the depth of planetary boundary layer as MLD in the analysis.

The model was integrated for 5 years archiving 5-day means. The simulated SSH anomalies were computed by removing the spatial mean of 4×4 degree grid boxes. The procedure for the chlorophyll anomaly computation follows that used in the satellite data but from simulated 5-day mean total chlorophyll concentrations. For Figures 1 and 2, the solutions were mapped to the same grid as the satellite SSH anomalies before computing the correlation.

Nutrient limitation

Phytoplankton growth rates in the ocean biogeochemistry component of the CESM are computed as

$$\mu_i = \mu_{i,ref} \cdot T_f \cdot V_i \cdot L_i \quad (1)$$

where μ_i is the C-specific growth rate (d^{-1}) for phytoplankton functional type (PFT) i , $\mu_{i,ref}$ is the maximum growth rate (referenced to 30°C), and T_f is the temperature limitation (“Q10”) function; V_i and L_i are the nutrient and light response functions, respectively [*Geider et al.*, 1998]. For diatoms (diat) and “small” phytoplankton (sp), the nutrient response function follows Liebig’s law of the minimum, such that the ultimate limitation term used to compute growth is that of the most limiting nutrient:

$$V_{diat} = \min(V_{diat}^N, V_{diat}^P, V_{diat}^{Fe}, V_{diat}^{Si}) \quad (2)$$

$$V_{sp} = \min(V_{sp}^N, V_{sp}^P, V_{sp}^{Fe}) \quad (3)$$

Evaluation of the Model Simulation

The eddy-rich 0.1° CESM has the sea surface height (SSH) variability that agrees well with the one estimated from space. Figure S1(a) shows the standard deviation of SSH in the observation from Collecte Localis Satellites (CLS/AVISO) that we used in this study. The regions of elevated SSH variability include the Antarctic Circumpolar Current (ACC), Brazil-Malvinas Confluence, Agulhas Current retroflection and East Australian Current. The model simulation captures not only the spatial pattern of elevated SSH variability but also the magnitude of it (Fig. S1(b)). The simulated chlorophyll (CHL) at the surface agrees with SeaWiFS observation to a somewhat lesser degree than SSH variability. Although it underestimates the CHL concentration, the model generally shows similar patterns of high CHL as satellite observations. The simulated iron also captures a large scale iron distribution in observations (Fig. S2).

Iron is the limiting nutrient in the south of ACC for all phytoplankton types in the model, hence the information of the iron meridional gradient is important to understand the chlorophyll variability associated with the mesoscale. In summer (January-March), the Indian-Pacific sector has little meridional gradient as iron is depleted by active primary production, which makes it unlikely that lateral advection such as through stirring and trapping are driving the iron anomaly in Fig 4a. In the Atlantic sector, however, iron concentration generally increases equatorward (Fig. S3(top)). Consistent with *in situ* observations [Bowie *et al.*, 2002], iron is supplied from the Patagonian Shelf to the northern ACC creating a meridional gradient in the model. Also, the dust input from the atmosphere is the greatest in the Atlantic sector [Luo *et al.*, 2008]. With increasing iron concentrations toward equator, the eddy-driven advection, as well as vertical mixing, can create iron perturbations associated with eddies.

In winter (July-September), the surface ocean features a higher iron concentration than in summer. The primary productivity is more regulated by the light availability, nevertheless the wintertime iron distribution shows how closely iron is linked to the vertical mixing, especially in the Indian-Pacific sector. There, deeper vertical mixing enriches the surface ocean with iron as indicated by the fact that higher concentration of iron collocates with the region of relatively deep mixed layers (> 50 m) (Fig. S3(bottom)). The mixed layer depth in the Indian-Pacific sector is spatially inhomogeneous, so there are larger horizontal iron gradients than in summer. As a result, it is more likely that the

eddy-driven advection sets the perturbations in iron, but vertical mixing modulation becomes larger than in summer at the same time. The Atlantic sector shows a meridional gradient of iron that is not different from summer.

The budget of the iron averaged over mixed layer

We analyzed the budget of iron ($fe(z,t)$) averaged over the mixed layer $H(t) = \eta(t) - h(t)$, where $\eta(t)$ is the sea surface height and $h(t)$ is the time-varying depth of the boundary layer determined by the KPP mixing scheme. The temporal evolution of the iron averaged over the mixed layer ($\langle Fe \rangle \equiv \frac{1}{H(t)} \int_{h(t)}^{\eta(t)} fe(z,t) dz$) can be written as

$$\begin{aligned} \frac{d\langle Fe \rangle}{dt} &= \frac{d}{dt} \left[\frac{1}{H(t)} \right] \int_{h(t)}^{\eta(t)} fe(z,t) dz + \frac{1}{H(t)} \int_{h(t)}^{\eta(t)} \frac{d}{dt} fe(z,t) dz \\ &\quad + \frac{1}{H(t)} \left[fe(\eta(t),t) \frac{d\eta(t)}{dt} - fe(h(t),t) \frac{dh(t)}{dt} \right] \\ &= \frac{1}{H(t)} \int_{h(t)}^{\eta(t)} \frac{d}{dt} fe(z,t) dz \\ &\quad + \frac{1}{H(t)} \left[(fe(\eta(t),t) - \langle Fe \rangle) \frac{d\eta(t)}{dt} - (fe(h(t),t) - \langle Fe \rangle) \frac{dh(t)}{dt} \right]. \end{aligned} \quad (4)$$

The first and second terms represent the mean tendency of iron in the mixed layer and the contribution by entrainment/detrainment, respectively.

The $fe(z,t)$ tendency in the model is computed as follows.

$$\begin{aligned} \frac{d}{dt} fe(z,t) &= -A_h(z,t) - \frac{\partial}{\partial z} (w(z,t) fe(z,t)) + \frac{\partial}{\partial z} \left(\kappa(z,t) \frac{\partial fe(z,t)}{\partial z} \right) \\ &\quad + F(z,t) + B(z,t), \end{aligned} \quad (5)$$

where A_h is the horizontal advection, w is the vertical velocity, $\kappa(z,t)$ is the vertical diffusivity, $F(z,t)$ is the surface iron flux (nonzero only at the surface) and $B(z,t)$ is the biological source/sink term. Using (5), (4) can be written as

$$\begin{aligned} \frac{d\langle Fe \rangle}{dt} &= \frac{1}{H(t)} \int_{h(t)}^{\eta(t)} \left[-A_h(z,t) - \frac{\partial}{\partial z} (w(z,t) fe(z,t)) \right] dz && \text{[3D adv]} \\ &\quad - \frac{1}{H(t)} \kappa(h(t),t) \frac{\partial fe(z,t)}{\partial z} \Big|_{z=h} && \text{[v. mix]} \\ &\quad + \frac{1}{H(t)} \int_{h(t)}^{\eta(t)} F(z,t) dz && \text{[flux]} \\ &\quad + \frac{1}{H(t)} \int_{h(t)}^{\eta(t)} B(z,t) dz && \text{[bio]} \\ &\quad + \frac{1}{H(t)} \left[(fe(\eta(t),t) - \langle Fe \rangle) \frac{d\eta(t)}{dt} - (fe(h(t),t) - \langle Fe \rangle) \frac{dh(t)}{dt} \right] && \text{[ent]} \end{aligned} \quad (6)$$

with the surface value of the diffusivity, $\kappa(\eta(t),t) = 0$.

Statistics

We constructed distributions of $\langle \text{Fe} \rangle$, $\langle \text{PAR} \rangle$ and the terms in (6) at the locations of anticyclones and cyclones in summer and winter along the ACC. Since not all distributions are normally distributed (e.g. $\langle \text{Fe} \rangle$), the median is used as a representative measure of the distributions. The medians of $\langle \text{Fe} \rangle$ and $\langle \text{PAR} \rangle$ distributions for anticyclones and cyclones in the ACC are first obtained. Then the differences in medians between anticyclones and cyclones are normalized by that appropriate to the entire ACC. In Figures 4a,c, we plot the percent value of the median differences.

The terms in (6) are normalized by the median of $\langle \text{Fe} \rangle$ along the entire ACC after being multiplied by 10 days, the time interval used in the tendency equation in the model. We then compare the medians of each term's distribution to quantify the systematic differences between anticyclones and cyclones in Figures 4b,d in the main article. The 95% confidence intervals are estimated using bootstrapping and are very close to the median itself due to a large sample size, hence they are not plotted in Figure 4. It is noted that the advection term includes all advective processes in the region whose absolute SSH anomaly exceeds 5 cm. Hence, it does not solely represent the advection by coherent eddy structures through stirring or trapping.

References

- Bowie, A., D. Whitworth, E. Achterberg, R. Mantoura, and P. Worsfold (2002), Biogeochemistry of Fe and other trace elements (Al, Co, Ni) in the upper Atlantic Ocean, *Deep-Sea Res. Pt I*, 49(4), 605–636.
- Campbell, J. W. (1995), The lognormal distribution as a model for bio-optical variability in the sea, *J. Geophys. Res.*, 100(C7), 13,237–13,254, doi:10.1029/95JC00458.
- Frenger, I. (2013), On Southern Ocean eddies and their impacts on biology and the atmosphere, Ph.D. thesis, ETH Zurich, Zurich, Switzerland, doi:10.3929/ethz-a-009938120.
- Garver, S. A., and D. A. Siegel (1997), Inherent optical property inversion of ocean color spectra and its biogeochemical interpretation: 1. time series from the sargasso sea, *J. Geophys. Res. Oceans*, 102(C8), 18,607–18,625, doi:10.1029/96JC03243.
- Gaube, P., D. B. Chelton, P. G. Strutton, and M. J. Behrenfeld (2013), Satellite observations of chlorophyll, phytoplankton biomass, and ekman pumping in nonlinear mesoscale eddies, *J. Geophys. Res. Oceans*, 118, 6349–6370, doi:

10.1002/2013JC009027.

- Geider, R., H. MacIntyre, and T. Kana (1998), A dynamic regulatory model of phytoplankton acclimation to light, nutrients, and temperature, *Limnol. Oceanogr.*, *43*, 679–694.
- Large, W., J. McWilliams, and S. Doney (1994), Oceanic vertical mixing: A review and a model with nonlocal boundary layer parameterization, *Rev. Geophys.*, *32*, 363–403.
- Luo, C., N. Mahowald, T. Bond, P. Y. Chuang, P. Artaxo, R. Siefert, Y. Chen, and J. Schauer (2008), Combustion iron distribution and deposition, *Global Biogeochem. Cycles*, *22*, GB1012, doi:10.1029/2007GB002964.
- Maritorena, S., D. A. Siegel, and A. R. Peterson (2002), Optimization of a semianalytical ocean color model for global-scale applications, *Appl. Opt.*, *41*(15), 2705–2714, doi:10.1364/AO.41.002705.
- Moore, J. K., S. C. Doney, J. A. Kleypas, D. M. Glover, and I. Y. Fung (2002), An intermediate complexity marine ecosystem model for the global domain, *Deep Sea Res., Part II*, *49*(1-3), 403–462.
- Moore, J. K., S. C. Doney, and K. Lindsay (2004), Upper ocean ecosystem dynamics and iron cycling in a global three-dimensional model, *Global Biogeochem. Cycles*, *18*, GB4028, doi:10.1029/2004GB002220.
- Moore, J. K., K. Lindsay, S. C. Doney, M. C. Long, and K. Misumi (2013), Marine ecosystem dynamics and biogeochemical cycling in the Community Earth System Model [CESM1(BGC)]: Comparison of the 1990s with the 2090s under the RCP4.5 and RCP8.5 scenarios, *J. Clim.*, *26*(23), 9291–9312, doi:10.1175/JCLI-D-12-00566.1.
- Siegel, D. A., S. Maritorena, N. B. Nelson, D. A. Hansell, and M. Lorenzi-Kayser (2002), Global distribution and dynamics of colored dissolved and detrital organic materials, *J. Geophys. Res. Oceans*, *107*(C12), 21–1–21–14, doi:10.1029/2001JC000965.
- Tagliabue, A., T. Mtshali, O. Aumont, A. Bowie, M. Klunder, A. Roychoudhury, and S. Swart (2012), A global compilation of dissolved iron measurements: focus on distributions and processes in the Southern Ocean, *Biogeosciences*, *9*, 2333–2349, doi:10.5194/bg-9-2333-2012.

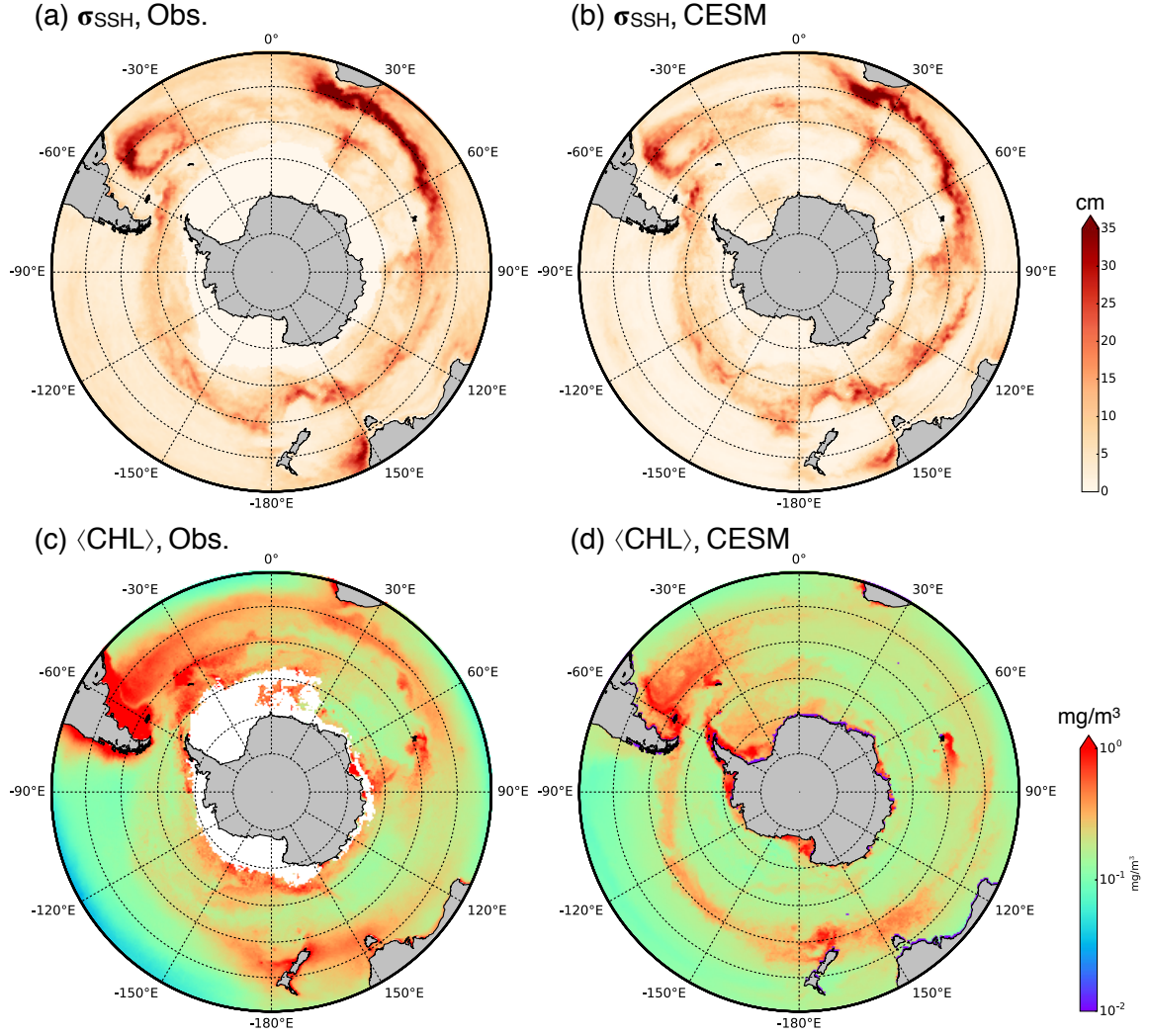


Figure S1. Standard deviation of sea surface height from (a) satellite observation and (b) eddy-resolving CESM. (c) and (d) show the time averaged surface chlorophyll estimated by ocean color and CESM, respectively. The white mask in (c) represents missing data.

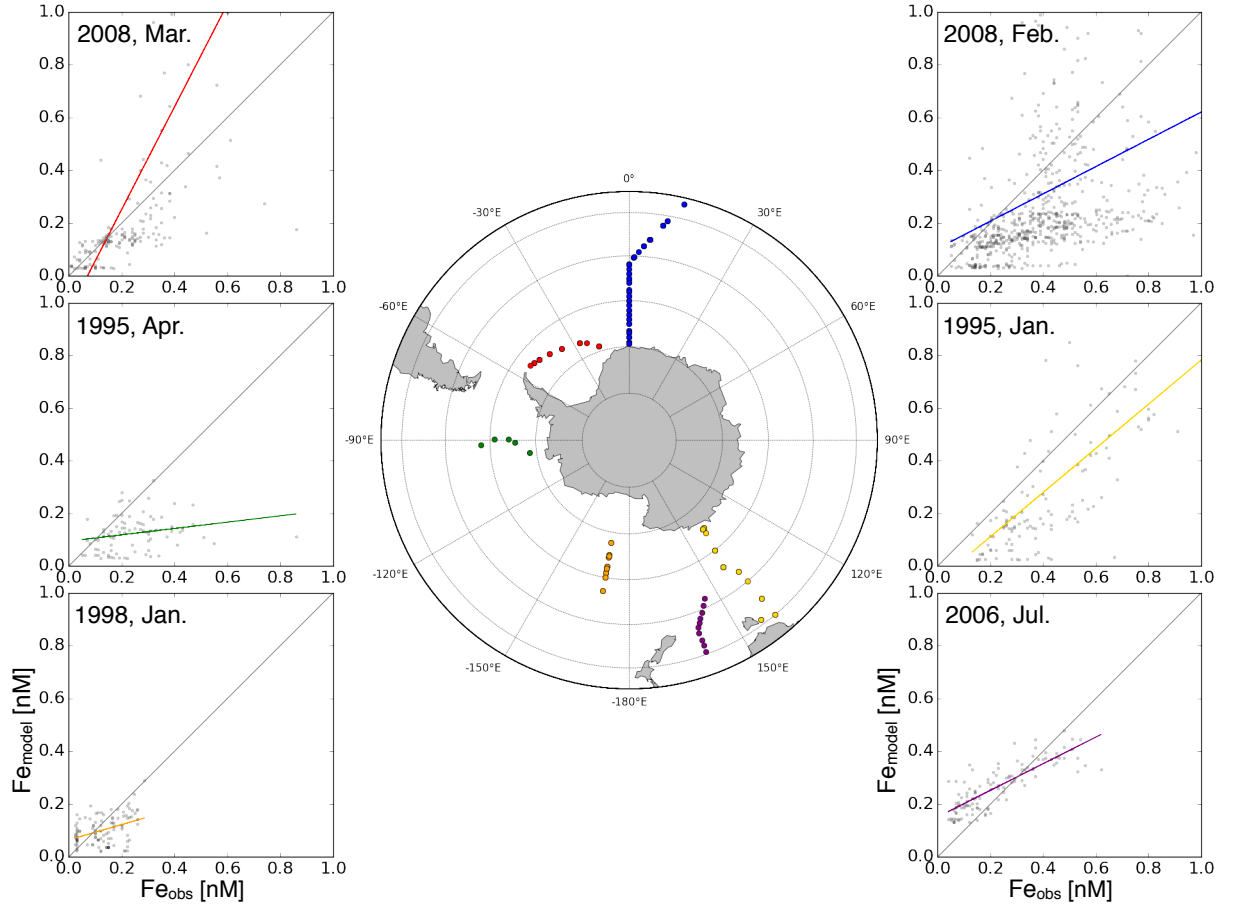


Figure S2. Dissolved iron data from observations and the model simulation is plotted along 6 transects in the SO. The observational data is taken from *Tagliabue et al. [2012]*. The colored lines are the linear least squares fit between the observations and the model data (gray dots), while gray lines are the one with a slope of 1. The colored dots on the map indicate the sampling location corresponding to the same colored line in the 6 panels.

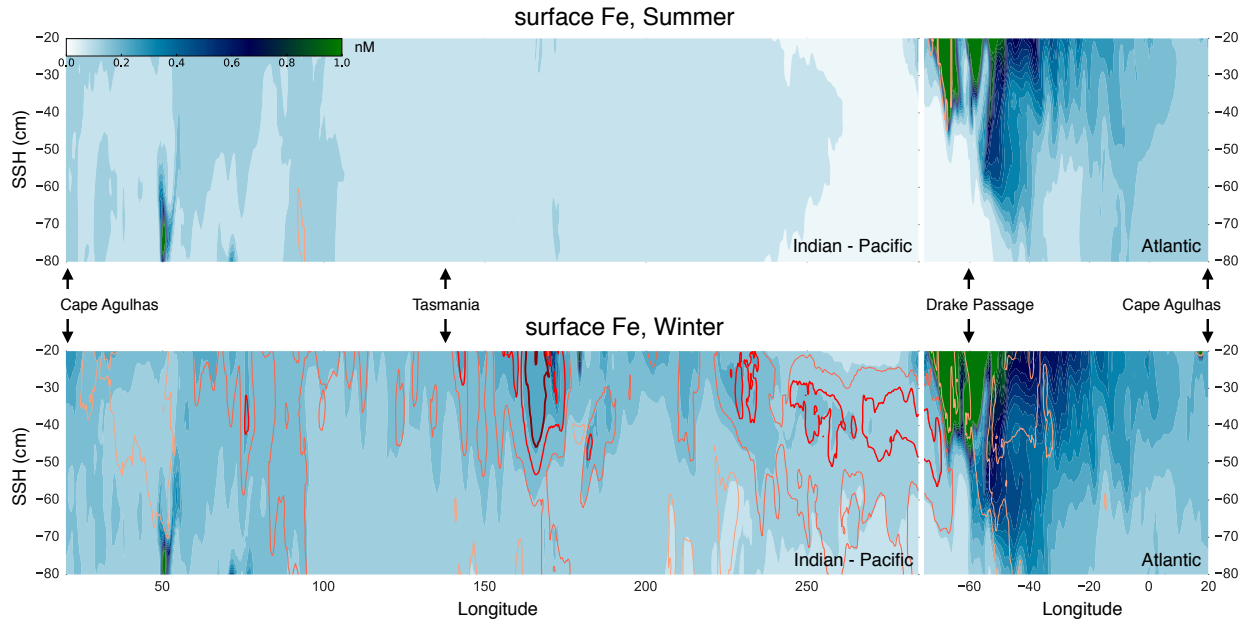


Figure S3. The shading is the seasonal mean iron along the SSH isolines for austral (top) summer and (bottom) winter computed in CESM. Orange, pink, red and dark red contours represent the regions with 50 m, 100 m, 150 m and 200 m levels of the planetary boundary layer depths estimated by the KPP vertical mixing scheme, respectively.